Supplementary Material

optica

Three dimensional biplane spectroscopic single-molecule localization microscopy

KI-HEE SONG,[1] YANG ZHANG,[1] GAOXIANG WANG,[2] CHENG SUN,[3] AND HAO F. ZHANG[1*]

[1]Department of Biomedical Engineering, Northwestern University, Evanston, IL 60201, USA
[2]Department of Hematology, Tongji Hospital, Tongji Medical College, Huazhong University of Science and Technology, Wuhan, Hubei, 430030, China
[3]Department of Mechanical Engineering, Northwestern University, Evanston, IL 60201, USA

Published XX Month XXXX

http://dx.doi.org/10.1364/optica.99.099999.s1 [supplementary document doi]

1. FOV characterization of 3D biplane sSMLM system

The usable field-of-view (FOV) is generally determined by the selection of the objective lens and the field of illumination. For sSMLM system, the FOV is further constrained by the diffraction angle (typically < 10 degrees) of the grating to avoid overlapping of the zeroth and the first order images. However, in the case of 3D biplane sSMLM method reported here, such constraint can be relaxed as the corresponding beam paths of the zeroth- and first-order images are manipulated independently. Assuming the illumination fully covers the entire FOV, the achievable FOV of our 3D biplane sSMLM using a 100x objective lens is ~ 40 × 40 μm^2. In this study, due to the constraint of illumination beam shape, the FOV of the acquired images was ~ 15 × 30 μm^2.

2. Spatial localization precision and spectral precision of 3D biplane sSMLM imaging

We first estimated the lateral localization precision in 3D biplane sSMLM using maximum-likelihood estimation (MLE) method as reported by Mortensen and Rieger [1, 2]:

$$\Delta x = \frac{F_{EM}\sigma^2 + a^2/12}{N}\left(1 + 4\tau + \sqrt{\frac{2\tau}{1+4\tau}}\right),$$

where $\tau = \frac{2\pi b(\sigma^2 + a^2/12)}{Na^2}$; F_{EM} is the noise factor when using the EMCCD camera (typically 2); σ is the standard deviation of a fitted Gaussian PSF in nm; a is the back-projected pixel size in nm; N is the number of photons detected for a given molecule; and b is the background photons. The expected lateral localization precision shown in Fig. S1(a) (blue solid line) was estimated based on Cramer–Rao lower bound (CRLB) using actual experimental conditions. In addition, we further quantified the lateral localization precision experimentally using far-red fluorescent nanosphere (200-nm diameter; F8807, Invitrogen™) as the test subject. By controlling the illumination power and integration time, we constrained the recorded photon numbers within the zeroth order image in the range of 500 to 1500, which corresponds to the photon number in our sSMLM measurements. We estimated the lateral localization precision using the standard deviation of 100 recorded image frames of the same far-red fluorescent nanosphere. As shown in Fig. S1(a), the experimentally obtained lateral localization precision agrees well with theoretical estimate.

Regarding the spectral precision, we have recently published the theoretical model in Ref. [3]. Using this model, the expected spectral localization precision is shown in Fig. S1(b) as blue solid line. In addition, we further quantified the spectral precision from the experimental data, which corresponds to the photon numbers in the range of 1500 to 4500 in the spectral image. As shown in Fig. S1(b), the experimental results agree-well with the theoretical estimation.

Finally, we estimated the axial precision with respect to the z position using a representative case marked as green circle shown in the inset in Fig. S1(a). Our established theoretical model for spectral precision [3] captures the localization precision in the spectral images. It can be further extended to the 3D biplane sSMLM imaging to estimate the axial precision based on a calibration measurement; we first obtained the sigma value of the PSF corresponding to different axial position from a calibration curve. Using this value, we generated spatial and spectral images in the numerical simulation reported in Ref. [3]. Then, we calculated the

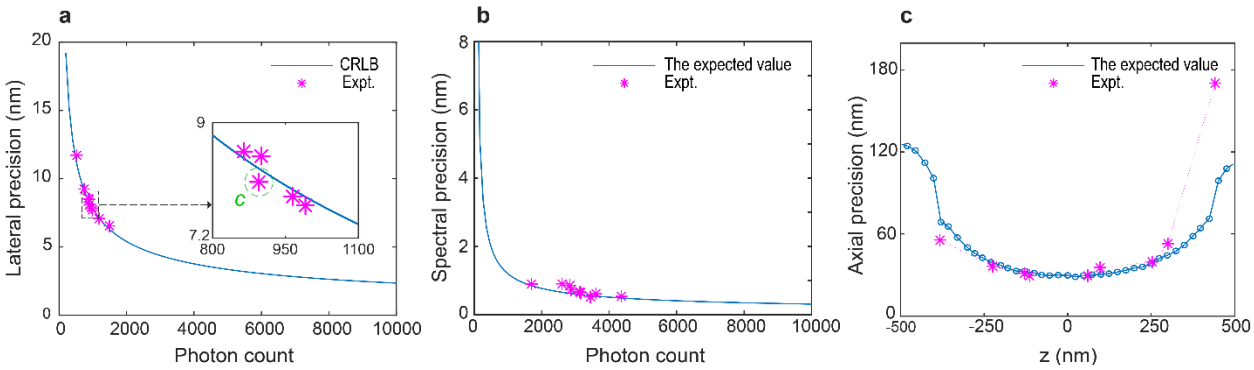

Fig. S1. (a) The lateral localization precision and (b) the spectral precision as a function of photon count. The blue lines in (a-c) represent the theoretically-expected values while the magenta symbols represent the experimentally-obtained values. We compared precisions at a single level of 500 photons to 1500 photons in spatial image corresponding to the actual signal level in our sSMLM system. Given a splitting ratio between zeroth order and first order of a grating, approximately 1 to 3, the corresponding signal level in spectral image was 1500 photons to 4500 photons. (c) The axial localization precision as a function of the z-position at the signal level of 900 photons corresponding to the green marker, *c* in the inset in (a). The background level, readout noise, and the spectral dispersion for theoretical estimation were 1 photon/pixel, 1e-/pixel, and 8 nm/pixel respectively in both analytical solution and numerical simulation.

axial precision at different axial position. As shown in Fig. S1(c), trends of experimentally observed axial precision at the different z-position follows the theoretical values well.

3. Comparison of spatial localization precision and spectral precision between 3D biplane- and astigmatism- based 3D sSMLM imaging

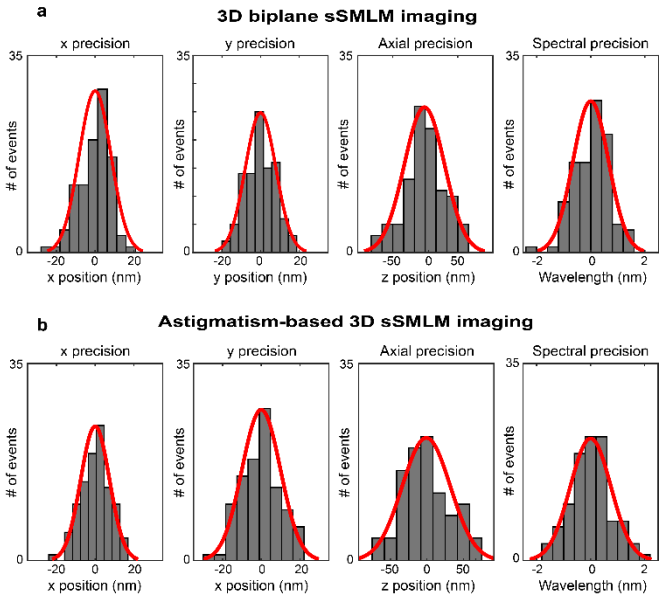

Fig. S2. Spatial localization precisions and spectral precision for (a) biplane- and (b) astigmatism- based 3D sSMLM imaging. We estimated the precisions using a standard deviation of 100 recorded image frames of a single fluorescent nanosphere. The red lines represent the fitted Gaussian curve of histograms. Its standard deviation indicates precision value.

To characterize the performance of three-dimensional (3D) biplane sSMLM system, we experimentally quantified the spatial localization precisions and spectral precision using fluorescent nanospheres and compared them with that of astigmatism-based 3D sSMLM. As shown in Fig. S2, both the biplane- and astigmatism-based approaches showed a comparable localization spatial precisions and spectral precisions. We found that the localization precisions along the x-axis are 8.25 nm and 7.42 nm, the localization precisions along the y-axis are 7.90 nm and 9.94 nm, and the axial localization precisions are 29.76 nm and 35.60 nm at ~ 900 photons for biplane- and astigmatism- based 3D sSMLM imaging methods, respectively. The spectral precisions are 0.66 nm and 0.75 nm at ~ 3000 photons for biplane- and astigmatism- based methods.

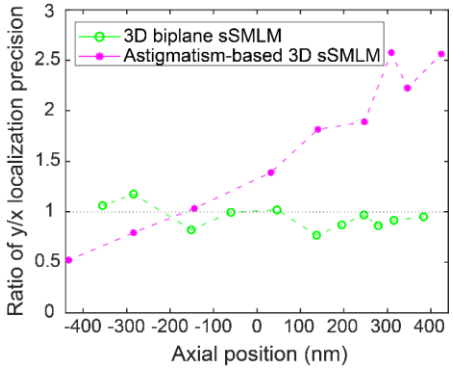

Fig. S3. Lateral precision isotropy variations as a function of axial positions in biplane- and astigmatism-based methods.

We further measured the depth variation of the ratio between the localization precisions along the x- and y-axis (defined as lateral precision isotropy) and compared the depth variations of the precision isotropy in both the biplane- and astigmatism-based methods. As shown in Fig. S3, the biplane-based method had a nearly uniform lateral precision isotropy within the entire 800-nm depth range. In contrast, the lateral precision isotropy varied significantly along the depth in the astigmatism-based method, due to non-uniform photon densities along the x and y axes induced by astigmatism. This is caused by changes in elongated PSFs as a function of the axial position, which affects the localization precisions along the x- and y-axis differently in the astigmatism-based method [4].

4. Estimation of misidentification of two dyes between two color channels

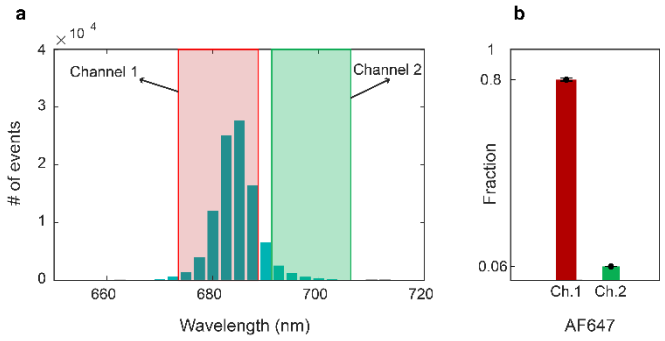

Fig. S4. (a) The histogram of centroid wavelengths of same single AF647 molecules in single-color 3D sSMLM imaging (b) The misidentification fraction of AF647 for the channel 2

We estimated misidentification of AF647 and CF660C between two color channels from statistical information obtained in the single-color 3D sSMLM imaging. We maintained similar experimental conditions, such as spectral dispersion, photon counts of emission, and the background level, between single-color and multi-color 3D biplane imaging experiments. To do this, we first randomly selected the centroid wavelengths of 1000 molecules among 99211 molecules and counted the number of centroid wavelengths categorized into each channel as shown in Fig. S4(a). Then, we calculated the misidentification fraction of AF647 for the channel 2. We repeated this estimation 50 times and calculated the mean value and its standard deviation (s.d.). We confirmed that the misidentification of AF647 for the channel 2 was 6.44 % with a s.d. of 0.65 % as shown in Fig. S4(b). Considering similar spectral variations of AF647 and CF660C in their centroid wavelengths [5], we assumed that misidentification of CF660c for the channel is also relatively insignificant.

5. Additional analyses of spatial localization precision and spectral precision obtained in 3D biplane sSMLM imaging

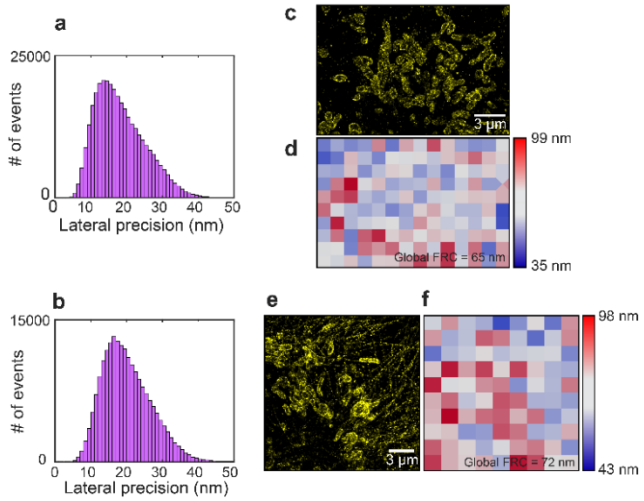

Fig. S5. Histograms of the lateral localization precision for (a) a single-color 3D sSMLM image and (b) a multi-color 3D sSMLM image. (c) A super-resolved image of Fig. 2(a) in the manuscript; (d) the corresponding local mapping of FRC values. (e) A super-resolved image of Fig. 4(a); (f) the corresponding local mapping of FRC values.

The estimation for the lateral localization precision was performed in ThunderSTORM plugin in ImageJ software [6]. We first obtained the histogram of the estimated lateral localization precision of individual molecules for single/multi-color 3D sSMLM images and calculated the average precision value. We obtained the average lateral localization precision of 18 nm for a single-color 3D sSMLM image and 20 nm for a multi-color 3D sSMLM image, together with the average intensity of 550 photons in the spatial image, as shown in Figs. S5(a) and S5(b) respectively.

In addition, we quantified the lateral resolution using the Fourier Ring Correlation (FRC) method [7-9]. We visualized the local FRC-estimated resolution of super-resolved images using NanoJ-Squirrel plugin in ImageJ software [8]. Figure S5(c) shows a superresolution image from Fig. 2(a) in the manuscript. The corresponding local mapping of FRC values is plotted in Fig. S5(d). The global FRC value was 65 nm and the minimum FRC value was 35 nm. Additionally, the superresolution image in Fig. 4(a) in the manuscript is shown as Fig. S5(e). Figure S5(f) shows the corresponding local mapping of FRC values. The global FRC value was 72 nm and the minimum FRC value was 43 nm. It should be noted that the final image resolution could be further affected by several other factors, such as biological drift, stage drift, density of fluorophores, and the photo-switching property of its blinking, as compared to the localization precision [7].

Next, spectral precision was quantified by precision in fitting the spectral centroids, which is determined as the standard deviation of the fitted Gaussian function. This value provides an insight to understand noise contribution to the spectral precision as well as a heterogeneity of spectroscopic signature of single molecules. We obtained a spectral precision of 4.21 nm for single-color 3D sSMLM imaging (corresponding to Fig. 2(i)), as shown Fig. S6(a). This value agrees with reported values in our previous work [10].

In addition, we measured the axial resolution, which can be empirically estimated by the localization distribution along the axial-axis from an isolated cluster from our multi-color 3D sSMLM images. We estimated the axial resolution from the full-width at half maximum (FWHM) of the distribution by $\Delta z = FWHM/2.35$, assuming the distribution follows a Gaussian distribution [11] as shown in Fig. S6(b). From the axial line profiles of microtubules near the region highlighted by the white-dashed line (Fig. 4(f)), we obtained the axial resolution to be ~ 50 nm.

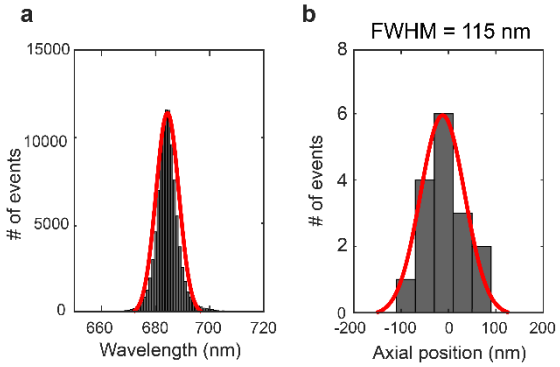

Fig. S6. (a) Histogram of the spectral centroid wavelength distribution extracted from a single-color 3D sSMLM image of Fig 2(i) (b) Histogram of the localization distribution in the axial-axis near the region highlighted by the white-dashed line (Fig. 4(f)) from a multi-color 3D sSMLM image.

6. Wavelength calibration challenge in the astigmatism-based 3D sSMLM system

The astigmatism-based 3D sSMLM system inherently suffers from a wavelength calibration challenge because the spatial and spectral imaging channels experienced different spherical aberrations, which is caused by inserting a cylindrical lens only into the spatial imaging (zeroth order) channel. This error may cause a significant spectral bias. To illustrate the spectral bias, we tested it using fluorescent nanospheres. We acquired 100 frames, which contained emission events of nanospheres, captured without and with a cylindrical lens. Fig. S7(a) shows the overlapped average image of 100 frames with the localization. The green and red colors in the spatial image (the orange dashed-box) represent the PSFs captured without and with the cylindrical lens, respectively, while the yellow color in the spectral image (the blue dashed-box) indicates their overlapped spectroscopic signatures. As a result, we observed different distances between the PSFs in the two situations. These differences in the spatial image introduced a wavelength calibration error up to 5 pixels (corresponding to 40 nm spectral bias) at the 8-nm/pixel spectral dispersion, as illustrated in Fig. S7(b). Such spectral bias can be worse in sSMLM systems with lower spectral dispersion and larger FOVs. Therefore, the astigmatism-based 3D method should not be directly applicable to sSMLM without careful spherical aberration compensation.

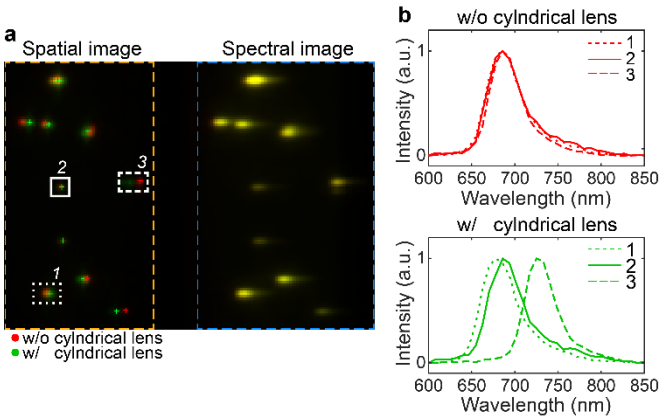

Fig. S7. Spectral bias caused by astigmatism. (a) The overlapped average image of 100 frames, which contain emission events of nanospheres in the spatial image (the orange dashed-box) and their spectroscopic signatures in the spectral image (the blue dashed-box), captured without and with a cylindrical lens. The green and red colors represent the PSFs in spatial images captured without and with the cylindrical lens, respectively, while the yellow color indicates their overlapped spectroscopic signatures. Their localized positions were marked with a plus symbol (+). The emission spectra corresponding to the PSFs in the white boxes captured without and with a cylindrical lens were visualized on the top and bottom in (b), respectively.

7. Ratio of FWHM of PSFs between spatial and spectral images for depth calibration

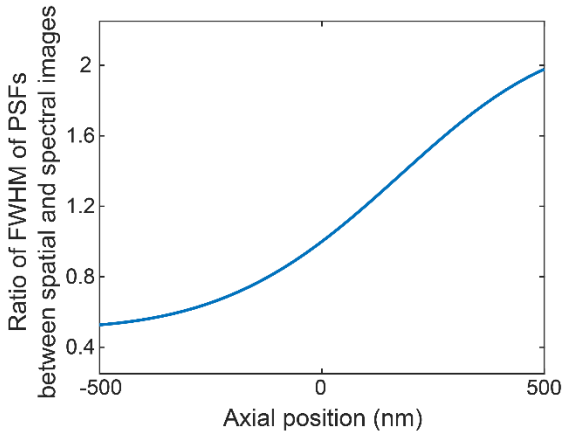

Fig. S8. Ratio of FWHM of PSFs between spatial and spectral imaging channels to be used for depth calibration in 3D biplane sSMLM.

REFERENCE

1. K. I. Mortensen, L. S. Churchman, J. A. Spudich, and H. Flyvbjerg, Nat Meth **7**, 377-381 (2010).
2. B. Rieger, and S. Stallinga, **15**, 664-670 (2014).
3. B. D. K. Song, C. Sun, and H. F. Zhang, Review of Scientific Instruments **89**, 123703 (2018).
4. M. F. Juette, T. J. Gould, M. D. Lessard, M. J. Mlodzianoski, B. S. Nagpure, B. T. Bennett, S. T. Hess, and J. Bewersdorf, Nat Methods **5**, 527-529 (2008).
5. Z. Zhang, S. J. Kenny, M. Hauser, W. Li, and K. Xu, Nat Methods **12**, 935-938 (2015).
6. M. Ovesny, P. Krizek, J. Borkovec, Z. Svindrych, and G. M. Hagen, Bioinformatics **30**, 2389-2390 (2014).
7. N. Banterle, K. H. Bui, E. A. Lemke, and M. Beck, Journal of Structural Biology **183**, 363-367 (2013).
8. S. Culley, D. Albrecht, C. Jacobs, P. M. Pereira, C. Leterrier, J. Mercer, and R. Henriques, Nature Methods **15**, 263 (2018).
9. R. P. J. Nieuwenhuizen, K. A. Lidke, M. Bates, D. L. Puig, D. Grünwald, S. Stallinga, and B. Rieger, Nature Methods **10**, 557 (2013).
10. Y. Zhang, K.-H. Song, B. Dong, J. L. Davis, G. Shao, C. Sun, and H. F. Zhang, Appl. Opt. **58**, 2248-2255 (2019).
11. A. Aristov, B. Lelandais, E. Rensen, and C. Zimmer, Nature Communications **9**, 2409 (2018).